

# Quantum correlation light-field microscope with extreme depth of field

Yingwen Zhang,<sup>1,2,\*</sup> Duncan England,<sup>2,†</sup> Antony Orth,<sup>2</sup> Ebrahim Karimi,<sup>1,2</sup> and Benjamin Sussman<sup>1,2</sup>

<sup>1</sup>*Nexus for Quantum Technologies, University of Ottawa, K1N 6N5, ON, Ottawa*

<sup>2</sup>*National Research Council of Canada, 100 Sussex Drive, Ottawa ON Canada, K1A0R6*

Light-field microscopy (LFM) is a 3D microscopy technique whereby volumetric information of a sample is gained by simultaneously capturing both the position and momentum (angular) information of light illuminating a scene. Conventional LFM designs generally require a trade-off between position and momentum resolution, requiring one to sacrifice resolving power for increased depth of field (DOF) or vice versa. In this work, we demonstrate a LFM design that does not require this trade-off by utilizing the inherent correlations between spatial-temporal entangled photon pairs. Here, one photon from the pair is used to illuminate a sample from which the position information of the photon is captured directly by a camera. By virtue of the strong momentum anti-correlation between the two photons, the momentum information of the illumination photon can then be inferred by measuring the angle of its entangled partner on a different camera. By using a combination of ray-tracing and a Gerchberg-Saxton type algorithm for the light field reconstruction, we demonstrate that a resolving power of  $5\ \mu\text{m}$  can be maintained with a DOF of  $\sim 500\ \mu\text{m}$ , approximately 3 times of the latest LFM designs or  $> 100$  time that of a conventional microscope. In the extreme, at a resolving power of  $100\ \mu\text{m}$ , it is possible to achieve near infinite DOF.

## I. INTRODUCTION

Utilizing the properties of quantum entangled photons to enhance the performance of sensing and imaging techniques has been an active area of research in recent decades. To date, most demonstrated techniques are focused on noise reduction in the low illumination regime by utilizing the strong correlations in one of the many degrees of freedom between entangled photon pairs, such as in time or position/momentum. Examples of this are sub-shot noise imaging [1, 2] and quantum ghost imaging [3–5]. Dispersion immune optical coherence tomography has also been demonstrated using the two-photon Hong-Ou-Mandel interference effect [6, 7]. With advances in detector technology, especially with the maturity of single photon sensitive event cameras [8, 9], it is now possible to simultaneously utilize the correlations between multiple degrees of freedom. It has been demonstrated for further enhanced noise reduction in imaging and sensing by utilizing spectral-temporal correlations [10] or spatial-temporal correlations [9, 11] in entangled photons. New quantum imaging techniques utilizing the quantum correlations in multiple degrees of freedom have also been demonstrated, such as snapshot hyperspectral imaging [12], phase imaging through phase contrast microscopy [13] and Fourier Ptychography [14], Hong-Ou-Mandel-microscopy [15], as well as light-field/plenoptic imaging [16]. In this work, we extend the quantum correlation light-field imaging design [16] to microscopy and demonstrate volumetric reconstruction of a microscopic scene at the few micron resolution with extreme depth of field (DOF).

Light-field or plenoptic imaging [17–19] is a class of imaging techniques which allows for the reconstruction of the light field through capturing both the position and momentum (angular) information of light rays simultaneously. With the reconstructed light field, volumetric information of an illuminated scene can be obtained in a single measurement, with no scanning required. This technique has been since adapted to microscopy [20, 21], and has been demonstrated in volumetric non-scanning imaging of neural activities [22], microendoscopy [23] and also shown to have potential applications in optogenetics [24]. Conventional light-field microscope (LFM) designs typically make use of a microlens array (MLA). By placing the MLA one focal length away from an image sensor, each microlens illuminates a subset of the pixels in the CCD. By knowing which lens the light ray enters, and onto which pixel it subsequently focuses, one can obtain both position and momentum information of the light ray simultaneously, at the expense of sacrificing spatial resolution to gain momentum resolution. Typical LFM designs have each microlens covering around  $10 \times 10$  pixels, thus resulting in a 10 times reduction to the position resolution and subsequently, resolving power. Increasing the size of each microlens to cover more pixels will increase the amount of momentum information captured and subsequently increase the DOF, however at the cost of further reduced position resolution. Techniques have been developed to improve either the DOF or resolving power such as through scanning the MLA [25] or the sample stage [26]. Others

---

\*Electronic address: yzhang6@uottawa.ca

†Electronic address: Duncan.England@nrc-cnrc.gc.ca

include applying 3D deconvolution [27], wavefront shaping [28], using a camera array [29], processing the light-field information through the Fourier domain [30], or using the aid of spherical aberrations in scanning LFM [31].

In recent years, a new light-field imaging technique using spatially correlated thermal or quantum light has been proposed [32–34]. Here one beam/photon illuminates a scene to capture the position information, and the momentum information is inferred from the correlated partner beam/photon that is measured on a separate camera. Using this method, no trade-off between the position and momentum resolution is needed since each beam can be captured on separate cameras thus allowing for a much larger DOF while not sacrificing resolving power. This technique, has since been demonstrated using weakly correlated thermal light [35, 36] and quantum-correlated light [16], with a DOF at around 10 mm for a resolving power in the order of  $100\ \mu\text{m}$ .

In this work, we present a proof-of-concept demonstration of light-field microscopy using quantum-correlated photons. We refer to this technique as quantum-correlation light-field microscopy (QCLFM) throughout the rest of the manuscript. Unlike the previous work [16] that only employed ray optics, we utilize a wave optics approach in order to account for the diffraction effects that result from the much smaller target features. Our results demonstrate a resolving power of  $5\ \mu\text{m}$  (200 lp/mm - line pairs per millimeter), with a depth of field (DOF) of  $\sim 500\ \mu\text{m}$ . At a resolving power of  $10\ \mu\text{m}$  (100 lp/mm), the DOF can be extended to over 1.5 mm. This DOF is  $> 100$  times that of a conventional microscope using the same objective lens. Compared to LFM designs, this is an order of magnitude larger compared to some of the earlier LFM demonstrations [27, 28] and is  $\sim 3$  times larger than some of the most recent LFM techniques [31]. In the extreme case, at a resolving power of  $100\ \mu\text{m}$ , we observed a nearly infinite DOF, a feat that is practically unfeasible with current LFM designs based on MLA. Limited by the single photon detection efficiency, the frame rate of QCLFM is currently in the order of 100 s per frame, much slower compared to conventional LFM designs that operate at 10-100 Hz. However, with expected advancements in single photon camera technology in the coming years, we are confident that QCLFM will become a potential alternative to conventional LFM designs.

## II. RESULTS

### A. Concept

The conceptual setup of the QCLFM system is shown in Fig. 1. Through the process of type-II spontaneous parametric down-conversion (SPDC), a high energy photon from a UV pump laser is converted into a pair of lower energy photons in a nonlinear crystal. The photon pairs have orthogonal polarization and are entangled in time, position and momentum. It is this strong correlation property of entanglement that is used to realize QCLFM. The photon pairs, named *signal* and *idler* are first separated into two paths via the use of a polarizing beamsplitter (PBS). In the path of the signal photon, the plane of the crystal is first imaged onto the sample placement region and then onto a time-tagging event camera to record the signal photon’s position information and arrival time. Through the path of the idler, the Fourier plane of the crystal is projected onto a different event camera to record the idler photons’ momentum information and subsequent arrival time. The photon pairs are then identified through a time-correlation analysis based on their detection time and the signal photon’s momentum information can then be inferred from its time-correlated partner.

The operation for digital refocusing of a sample placed out of focus by a distance  $z$  can be achieved using two steps. First, using the position and momentum information of each photon, and knowing the optical elements used between them, the trajectory of the photons can be reconstructed through a ray tracing operation. For large features, where diffraction effects are negligible, this first step, using ray optics, is enough to bring the sample back into focus [16], however, for smaller features, interference and diffraction effects from wave optics must also be taken into account. In this case, the image obtained after ray tracing is the diffraction pattern amplitude of the sample at a distance  $z$  when illuminated by a plane wave propagating in the  $z$ -direction (see the Supplementary for details). The second step is to use a Gerchberg-Saxton type algorithm [37, 38] to recover the amplitude of the sample. This refocusing process is illustrated in Fig.2. Details on the experimental setup and the refocusing procedure can be found in the Methods section.

### B. Experimental Results

For this experiment, only a single time-tagging event camera ( $256 \times 256$  pixels with  $55\ \mu\text{m}$  pixel pitch) is used. A corner of the camera of around  $100 \times 100$  pixels was used for momentum measurement with the rest of the camera used for position measurement. With the momentum correlation of the photon pair measured to be approximately 2 pixels wide ( $13.6 \times 10^{-3}\ \mu\text{m}^{-1} / 17.6 \times 10^{-4}\ \text{rad}$ ), effectively around  $50 \times 50$  pixels are used for momentum measurement. Though the idler beam is overlapped with part of the signal beam on the camera, since a coincidence measurement

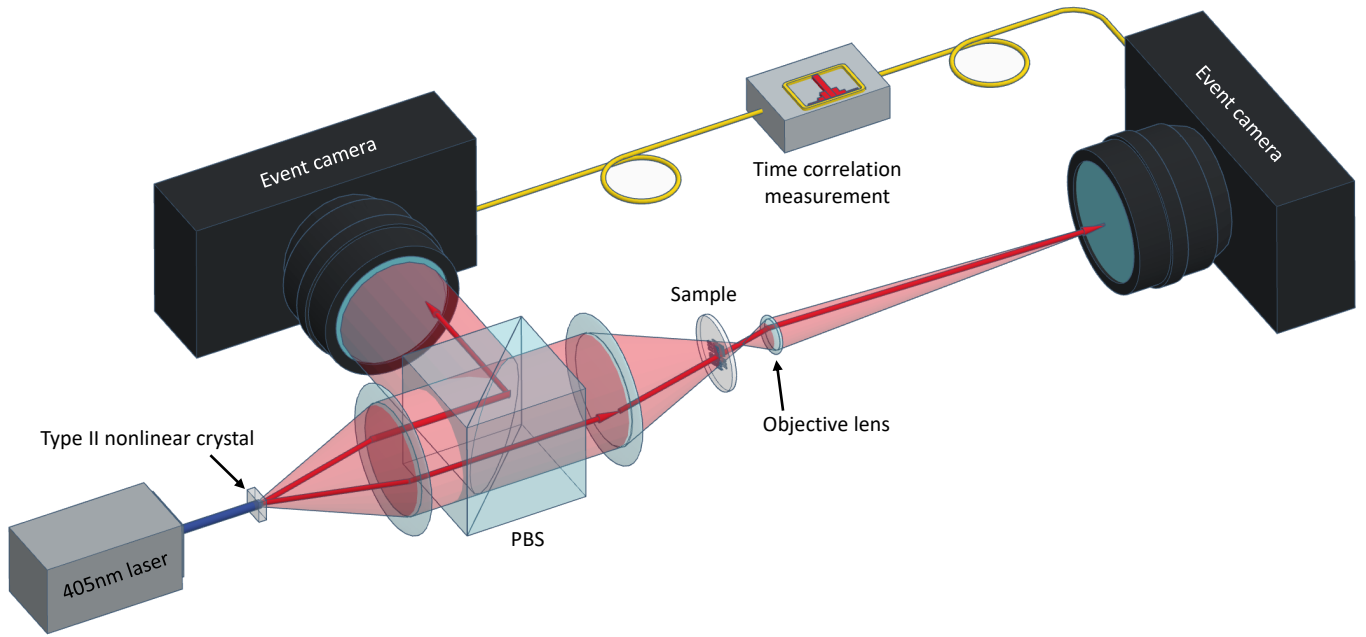


FIG. 1: **Conceptual setup of the QCLFM system.** Pairs of photons with orthogonal polarization, correlated in time, position and momentum, are generated through the process of type II SPDC. The photon pairs, *signal* and *idler*, are separated into two separate paths via the use of a polarizing beamsplitter (PBS). In the signal path, the plane of the crystal is first imaged onto the sample placement region and then onto a time-tagging event camera where position information of the photons are captured. In the idler path, the Fourier plane of the nonlinear crystal is projected onto a different event camera to record the partner photons' momentum information. Time correlation measurements are then performed on all photons detected on the two cameras to identify the photon pairs. The momentum information of the signal photon can then be inferred from its time-correlated partner.

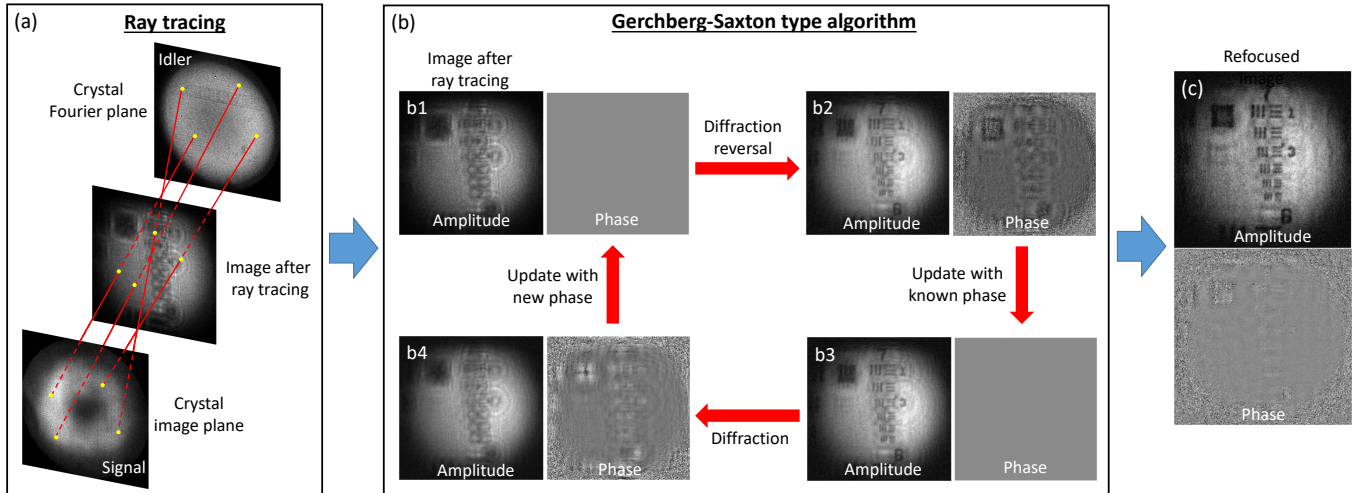
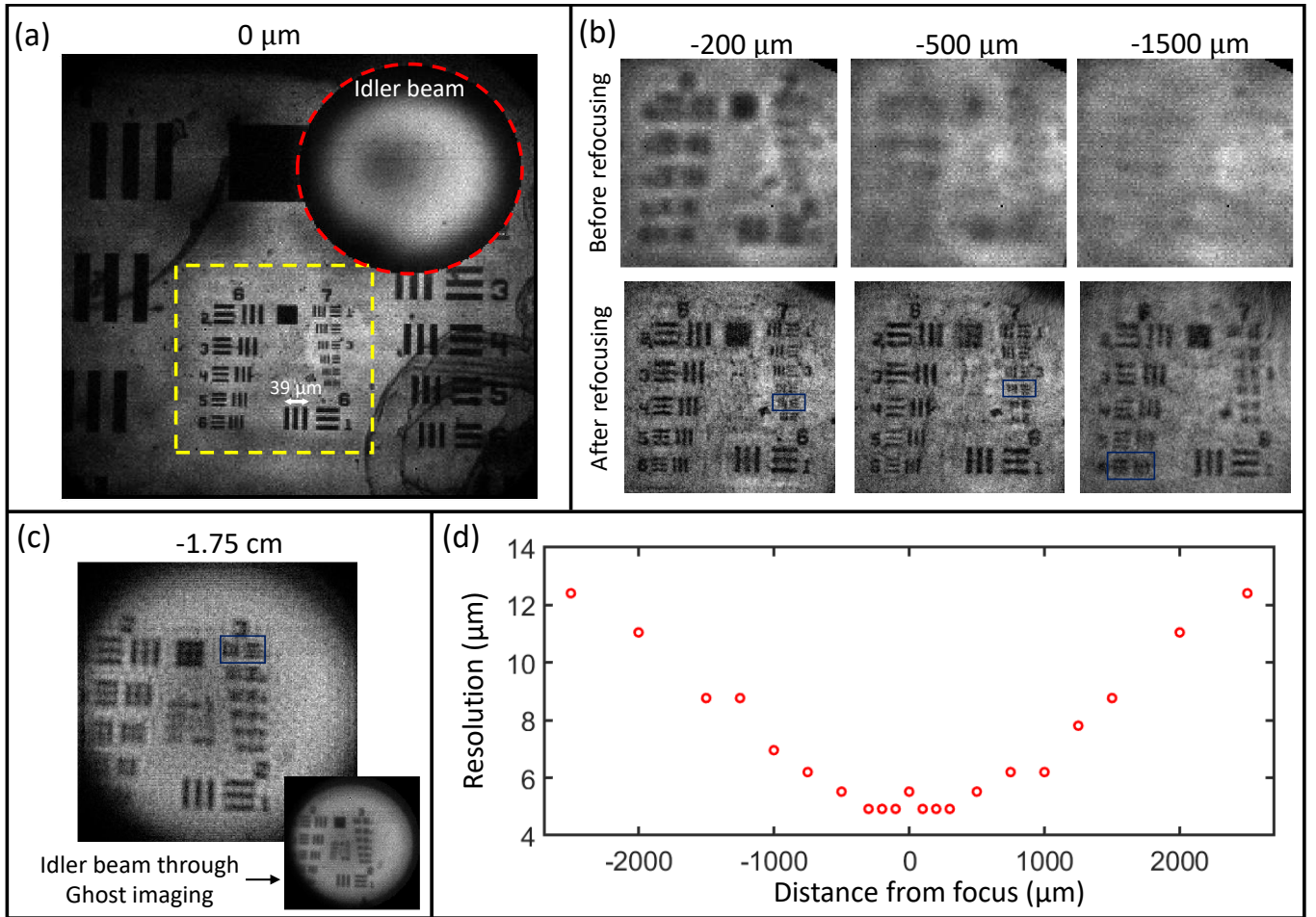


FIG. 2: **Illustration of the digital refocusing process.** (a) Using the photon pairs locations detected on the nonlinear crystal's image plane and Fourier plane, a ray-tracing approach is first used to obtain the diffraction pattern amplitude of the sample as if illuminated by a plane wave propagating in the  $z$ -direction. (b) For a sample of uniform or known phase profile, a Gerchberg-Saxton type algorithm is used to recover the amplitude profile of the sample. (c) The recovered amplitude and phase of the sample after 10 loops in the algorithm. This illustration is that of a 1951 USAF resolution target (group 7) placed at  $z = -300 \mu\text{m}$  away from the focus of the microscope objective.



**FIG. 3: Refocusing of 1951 USAF resolution target** (a) Image of a 1951 USAF resolution target, obtained after time correlation measurement, placed in the focus of a  $20\times$  0.45 NA objective lens. Here, for every photon detected in the idler beam, there is a signal photon detect in coincidence in the rest of the image. The region circled in red is the far field imaged by the idler photons. To not overshadow the rest of the image, the idler beam is only displayed at 30% intensity. (b) Before and after images of digitally refocusing groups 6 and 7 of a 1951 USAF resolution target (region in green square of (a)) placed at different distances from the objective focus with the smallest resolvable features after refocusing are boxed in blue. The data acquisition time for the images is 200 s. (c) Digital refocusing of USAF target groups 2 and 3 placed 1.75 cm away from the focus with a slightly different lens configuration. This is very close to the Fourier plane as the target can be clearly seen through ghost imaging in the idler beam (inset). See the main text for an explanation of ghost imaging. (d) Plot of the smallest resolution that can be refocused as a function of the distance a target is placed away from the focus with positive distance being towards the objective and negative away from the objective. The small peak at  $0\ \mu\text{m}$  is a consequence of clustering in the raw camera data, see the Methods section for more details on this. For images of the full dataset of (b) and (c), see the Supplementary.

is performed, the noise in accidental coincidences from this overlap is negligible. This is based on the fact that the probability of having two signal photons generated within the coincidence gating time of 10 ns is very low. See the Method section for more details.

In Fig. 3 we show digitally refocused images of a 1951 USAF resolution target placed at different distances from the objective focus. We see that a line spacing of  $5\ \mu\text{m}$  (group 7 element 5) can still be brought back into focus when the target is placed  $\pm 500\ \mu\text{m}$  away from the focus of the objective lens (positive being towards the objective lens and negative being away from) and for a line spacing of  $10\ \mu\text{m}$  (group 6 element 5) this distance can be extended to more than  $1500\ \mu\text{m}$ . In the extreme case, we are able to refocus a target placed at  $-1.75\ \text{cm}$  away from the focus with a line spacing of  $\sim 100\ \mu\text{m}$ , as seen in Fig. 3(c) which is very close to the Fourier plane, i.e. near infinity. This is verified through ghost imaging [3–5], a correlation imaging technique using pairs of photons, in which the idler photon does not interact with the target being imaged, with only the signal photon interacting with the target. By time correlating the detection events of the two photons, an image of the object will appear through the idler photons even though

they did not directly interact with the target. Knowing the idler beam is imaged in the crystal’s Fourier plane, being able to see the target clearly after time correlation measurement is an indicator that the target is also placed at/near the Fourier plane.

Comparing to MLA based LFM demonstrations with a similar resolving power, we achieved around an order of magnitude improvement in DOF as compared to earlier LFM demonstration [27, 28] (group 7 element 3 with  $1000\ \mu\text{m}$  DOF compared  $100\ \mu\text{m}$  DOF), and  $\sim 3$  times improvement in DOF compared to one of the latest LFM demonstrations [31] (group 7 element 3 with  $1000\ \mu\text{m}$  DOF compared to  $300\ \mu\text{m}$  DOF and group 6 element 3 with  $2000\ \mu\text{m}$  DOF compared to  $800\ \mu\text{m}$  DOF), all of which uses more sophisticated techniques such as deconvolution, wavefront shaping and spherical aberration assistance for improving position resolution and DOF. In addition, we see that QCLFM is also insensitive to the direction at which the target is placed from the objective focus as compared to some conventional LFM techniques [27, 31]. On the other hand, a conventional microscope with an objective numerical aperture of 0.45, as used in this experiment, would have a depth of field of approximately  $5\ \mu\text{m}$  (see Supplementary materials for details).

Next, we test our technique on a more complex 3D scene. Imaging of multiple overlapping fiber strands, between  $5 - 10\ \mu\text{m}$  in diameter, on the edges of a  $\sim 3\ \text{mm}$  thick stack of lens-cleaning tissue can be seen in Fig. 4. A single measurement was taken on the stack of lens tissue with digital refocusing performed in post-processing. We can see fiber strands more than  $1\ \text{mm}$  away from the objective lens focus, and completely not visible at the objective focus, being brought back into focus. The post-processing results in a stack of in-focus images obtained at various depths in the sample, some examples of which are shown in Fig. 4(a). The sum of all of these depth images results in an “all in focus” image (Fig. 4(b)) in which every strand, regardless of its position, is brought into focus. Finally, by colour-coding each image based on its depth, we generate a depth map of the 3D scene shown in Fig. 4(c).

Some artifacts/halos can be seen in the refocused images, this is likely a result of wavefront distortions from the multiple lenses used in the setup which were not taken into account during the refocusing procedure. Another likely source is in the approximations made in the refocusing procedure, such as small angle approximations and the uniform illumination beam intensity (see the Supplementary for details).

### III. DISCUSSION

We have made a proof-of-concept demonstration of a LFM design based on utilizing the inherent position and momentum correlation of entangled photon pairs generated through the process of SPDC. Since each degree of freedom can potentially be measured on separate cameras, one does not need to sacrifice position resolution for momentum resolution or vice versa as in conventional LFM designs. This has allowed us to achieve a DOF that is approximately 3 times larger than that of the latest LFM designs, all at an illumination power of about  $3\ \text{pW}$  ( $15 \times 10^6$  photons per second at  $810\ \text{nm}$ ). With the high momentum resolution (effectively  $\sim 50 \times 50$  pixels at  $13.8\ \mu\text{m}^{-1}$  per pixel), it is even possible to digitally refocus objects placed at near infinity, though with a moderate resolving power. In addition, as compared to some conventional LFM techniques, QCLFM is also insensitive to whether the target is placed before or after the objective focus.

The DOF can be further increased if a higher degree of momentum correlation is achieved with a separate camera used for the momentum measurement on the idler photon. Momentum correlation can be improved by increasing the pump beam waist or using a pump with a longer coherence length. Details on this can be found in the Methods section. Position resolution can be further improved by a factor of 3 on the event camera (TPX3CAM) using centroiding techniques [39]. QCLFM only utilizes the strong correlations inherent in spontaneous parametric downconversion, and does not leverage photon entanglement. Thus it is possible to imagine combining QCLFM with other quantum sensing techniques which directly utilize entanglement, such as quantum lithography [40, 41], to achieve resolution beyond the diffraction limit. Additionally, the current QCLFM design is still in its most basic form, we believe significant performance gains can be made by incorporating more sophisticated techniques already developed for the conventional LFM design such as 3D deconvolution and wavefront shaping.

One limitation of the current QCLFM design and refocusing algorithm is that it can only be used for targets with a known or constant phase profiles. A potential method to solve this is to also capture the beam in an intermediate plane in addition to just the near and far field. With this extra information one may be able to determine both the amplitude and phase of the diffraction pattern of the sample at two different planes from which the phase and amplitude of the sample can be retrieved. The feasibility of this approach will require further investigation. Another limitation to the technique’s performance (and all single photon quantum imaging techniques in general) is in its slow data acquisition speed, which is in the order of a few hundred seconds per frame as compared to the  $10\text{-}100\ \text{Hz}$  frame rate of classical LFM designs. This is mainly limited by the detection efficiency and timing resolution of the detection camera. The single photon detection efficiency of the camera used here is  $\sim 7\%$  with an effective timing resolution of  $\sim 8\ \text{ns}$  [42]. Since the pair detection efficiency is quadratic with respect to the single photon detection efficiency, with a



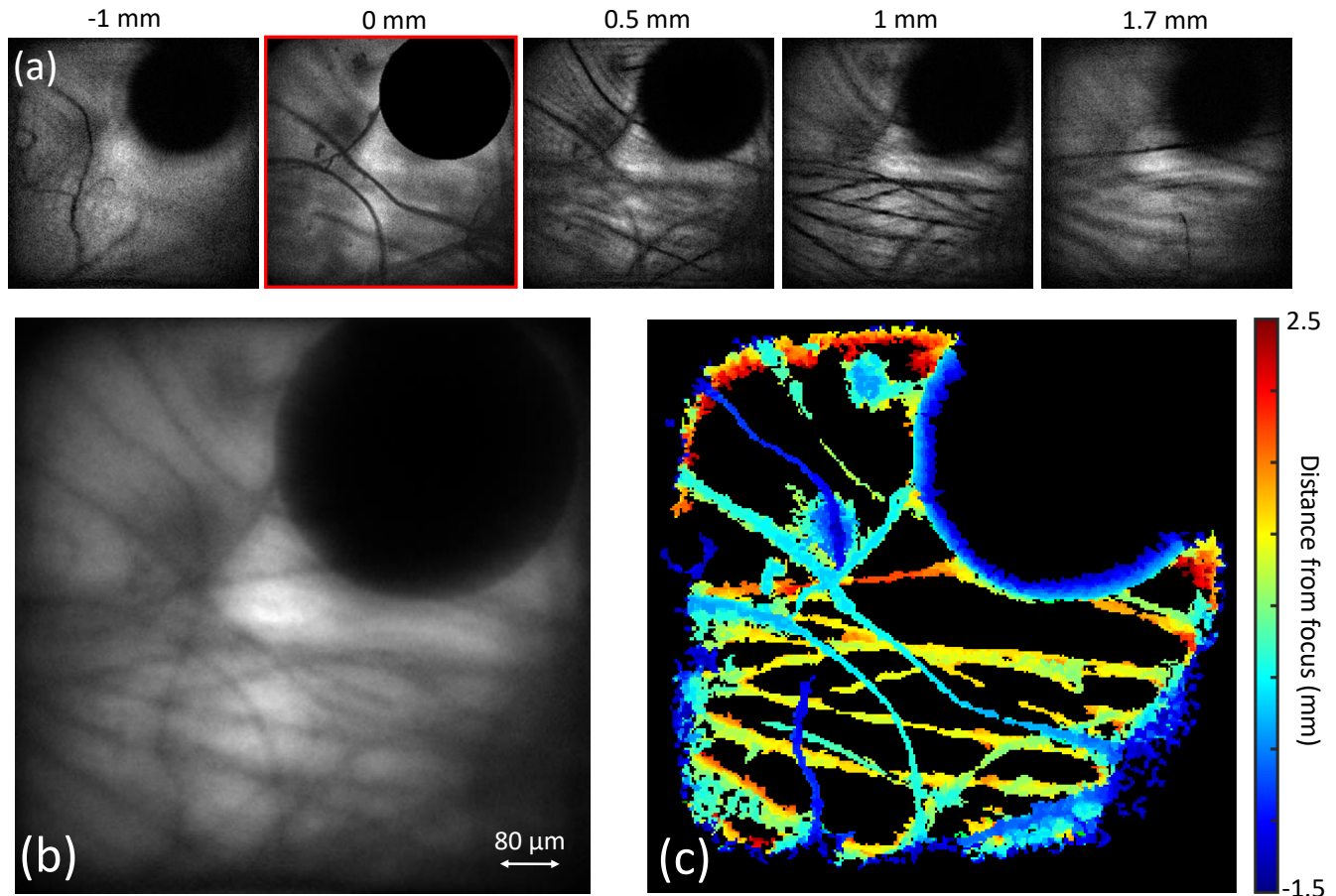


FIG. 4: **Refocusing of lens tissue fiber** (a) Digitally refocusing onto fiber strands of lens-cleaning tissue at various distances from the focus of the objective lens. The image at the lens focus is highlighted in red. The fiber strands are from the edges of a  $\sim 3$  mm thick stack of lens cleaning tissue. The measurement is taken in with a data acquisition time of 200 s. The empty circular region on the top right is the part of the camera used for capturing the idler photons. (b) Image showing all fiber strands brought into focus through post-processing. (c) Depth map of the fiber strands. A video showing the refocused images at different depths can be found in the Supplementary.

camera efficiency of 50%, we could expect a  $(50/7)^2 \approx 50$  times improvement in the data acquisition speed. Moreover, the signal-to-noise ratio of temporal correlation measurement scales as the square-root of the timing resolution, so if a timing resolution of 0.1 ns can be achieved, a further 10 times reduction to the data acquisition time is possible. Single-photon avalanche photodiode array cameras meeting these specifications are currently in development and may become commercially available soon [43]. We expect this makes real time imaging and microscopy with QCLFM (and many other quantum imaging techniques) a possibility in the near future.

#### IV. METHODS

##### Experimental Setup

The schematic of our QCLFM setup is shown in Fig. 5(a). A fiber coupled 405 nm continuous wave (CW) laser, at  $\sim 30$  mW, is used to pump a  $1 \times 2 \times 1$  mm (H $\times$ W $\times$ L) Type II periodically-poled potassium titanyl phosphate (ppKTP) crystal to produce entangled photon pairs through SPDC, at a rate of approximately  $15 \times 10^6$  photon pairs per second or, after accounting for the 7% camera detection efficiency, about 15 photons per second per pixel detected on the camera. The photon pairs are orthogonal in polarization, correlated in position, momentum and time. The SPDC photons are then separated by a polarizing beam splitter (PBS) into two paths. In the path of

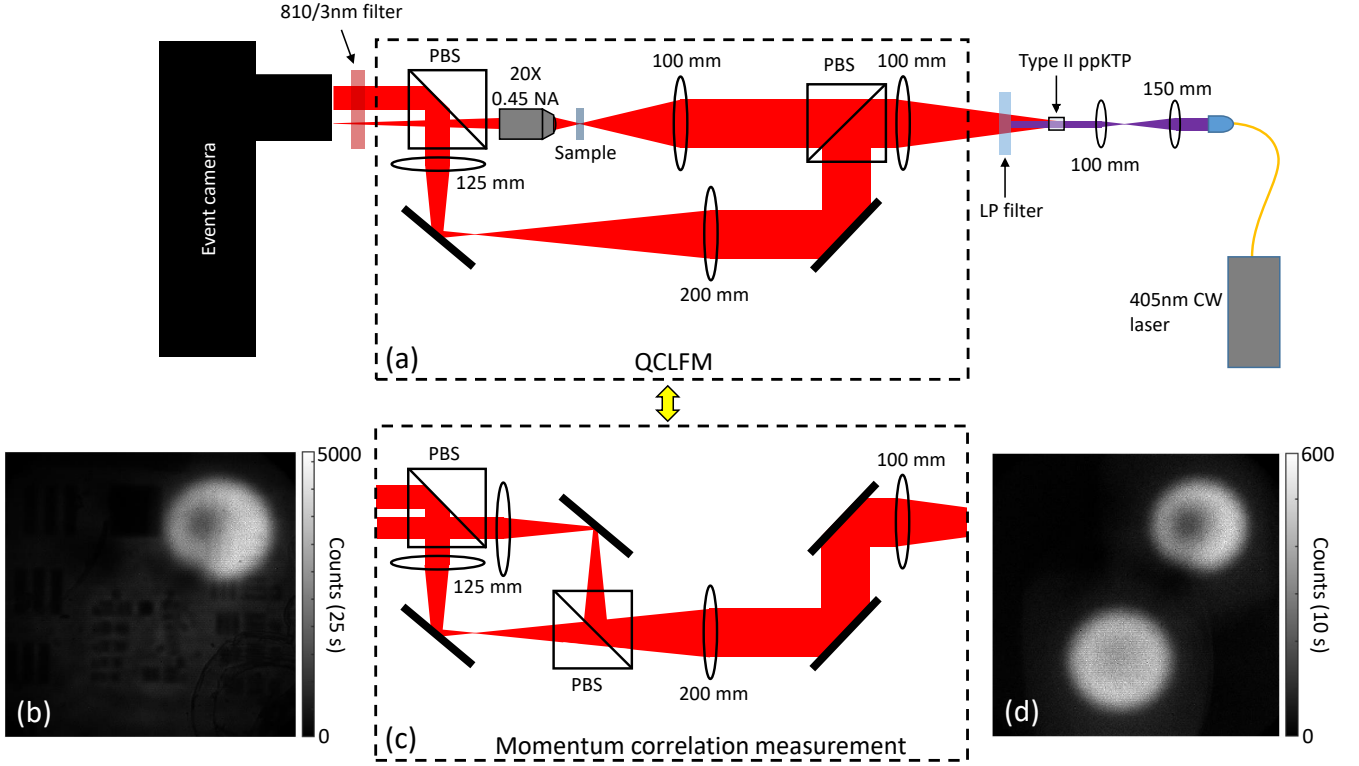


FIG. 5: **Experimental setup of QCLFM** (a) Experimental setup of the QCLFM. PBS: polarizing beamsplitter, LP filter: longpass filter. (b) A typical image captured on the camera, before time correlation analysis, accumulated over 25 s, of a 1951 USAF resolution target placed 200  $\mu\text{m}$  away from the objective focus. The signal beam covers the whole sensor area, while the idler is the bright region on the top-right corner. (c) The modified experimental setup for performing momentum correlation measurement. (d) Image captured on the camera, before time correlation analysis, accumulated over 10 s, for performing momentum correlation measurement. The darker patch seen in the idler beam in both (b) and (d) is due to a damaged region on the camera system resulting in lower detection efficiency.

the signal photon, the plane of the crystal is first imaged onto the sample placement region and then onto a time-tagging event camera (TPX3CAM [8, 44]) to record the signal photon's position information and arrival time. In the path of the idler photon, the Fourier plane of the crystal is projected onto a corner of the camera to record the idler photons' momentum information and the subsequent arrival time. Thus, the position information of the signal photon is captured directly and its momentum information can be inferred from the idler partner. The photon pairs are identified through a time correlation measurement, with a coincidence gating time of 10 ns, on all photons detected between the idler beam region and the rest of the camera. A typical image captured, before time correlation analysis, can be seen in Fig. 5(b). The idler beam on the corner is seen much brighter compared to the signal beam covering the whole sensor, this is due to a similar amount of photons being concentrated onto a smaller area.

The TPX3CAM has  $256 \times 256$  pixels with a pixel pitch of  $55 \mu\text{m}$ . The pixels can individually time the arrival time of a light pulse with 1.6 ns accuracy. The camera is made single photon sensitive with an attached image intensifier in which a single photon is converted into a flash of light bright enough to be registered by the camera. The flash of light will illuminate a small cluster of pixels on the camera, on which a clustering identification and centroiding algorithm must be implemented to regroup each cluster into a single event. A consequence of the clustering is a slight blurring of the raw image data, resulting in it being difficult to find the objective focus precisely. This is what resulted in the slight decrease in resolution at  $0 \mu\text{m}$  seen in Fig. 3(d). The timing of the camera pixels is intensity dependent, in which brighter pixels of a cluster will be registered as an earlier event than dimmer pixels of the same cluster, even though they are created from the same single photon event. This intensity-dependent timing must also be corrected and will result in losing some timing accuracy giving an effective timing accuracy of  $\sim 8$  ns. The quantum efficiency of the camera system (camera + intensifier) was measured to be  $\sim 7\%$ . More details on the camera and the post-processing required can be found in [42, 45].

The lenses in the signal beam were chosen such that the signal beam is not too tightly focused onto the sample region, allowing the field of view to stay roughly constant in the region of  $\sim \pm 2$  mm from the objective focus. When

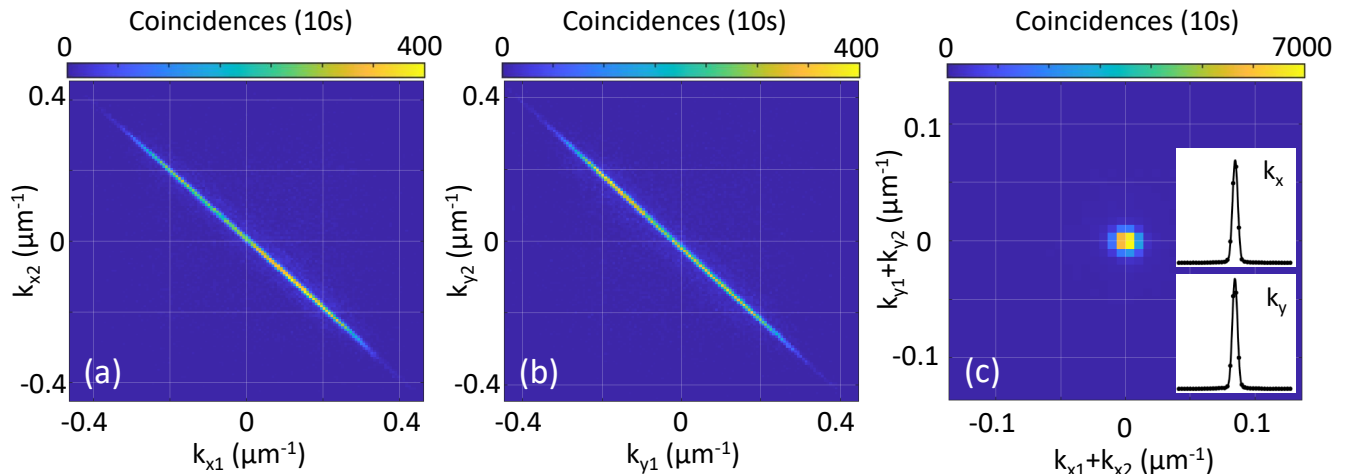


FIG. 6: **Momentum correlation measurement** (a) Joint probability distribution of photon momentum in the x-direction  $k_x$ . (b) Joint probability distribution of photon momentum in the y-direction  $k_y$ . (c) Sum coordinate projection of the joint probability distribution with the fitted Gaussian to the cross-section of the  $k_x$  and  $k_y$  direction shown in the inset. Fitted Gaussian gives  $\sigma_{k_{x1}+k_{x2}} = 6.1 \times 10^{-3} \mu\text{m}^{-1}$  (0.90 pixels) and  $\sigma_{k_{y1}+k_{y2}} = 6.4 \times 10^{-3} \mu\text{m}^{-1}$  (0.93 pixels).

magnified onto the camera, the beam size should also roughly match the sensor area of the camera to ensure most photons will be captured. Likewise, in the idler beam, the lenses were chosen such that the idler beam will cover roughly a region of  $100 \times 100$  pixels of the camera.

In order to achieve the highest degree of momentum correlation possible, a pair of lenses with focal length 100 mm and 150 mm were used to collimate and demagnify the laser beam to  $\sim 1$  mm in diameter when hitting the ppKTP crystal. The expected degree of momentum correlation can be calculated as [46]

$$\sigma_{k_1+k_2} = \sqrt{1/l_c^2 + 1/(4\omega_p^2)}, \quad (1)$$

where  $\sigma_{k_1+k_2}$  is the standard-deviation in the momentum correlation between two photons with momentum  $k_1$  and  $k_2$ ,  $l_c$  is the coherence length of the pump laser and  $\omega_p$  is the pump beam waist radius at the crystal. For our pump laser,  $l_c \approx 200 \mu\text{m}$  and  $\omega_p \approx 500 \mu\text{m}$ , thus giving  $\sigma_{k_1+k_2} \approx 5 \times 10^{-3} \mu\text{m}^{-1}$ .

The experimental setup to perform momentum correlation measurement is shown in Fig. 5(b). Here, the Fourier plane of the crystal is imaged by both the signal and idler photons, each onto a separate region of the camera. The common 200 mm lens is moved along the beam path until the highest degree of momentum correlation is observed. This setup is designed such that alteration of the idler path is kept to a minimum when converting to the QCLFM setup of Fig. 5(a). Momentum correlation measurement should be performed first in order to ensure that when converted to QCLFM, the camera is imaging the exact Fourier plane of the crystal which would contain the highest degree of momentum correlation.

The measured momentum correlation, determined by fitting a Gaussian of the form  $f(k) = a \exp\left(-\frac{(k-b)^2}{2\sigma_{k_1+k_2}^2}\right)$  to the central peak of the sum coordinate projection of the momentum joint probability distribution seen in Fig. 6(c), is  $\sigma_{k_{x1}+k_{x2}} = 6.1 \times 10^{-3} \mu\text{m}^{-1}$  (0.90 pixels) and  $\sigma_{k_{y1}+k_{y2}} = 6.4 \times 10^{-3} \mu\text{m}^{-1}$  (0.93 pixels) in the x and y direction respectively. This is in agreement with the expected  $5 \times 10^{-3} \mu\text{m}^{-1}$  as calculated using Eq. (1).

The achievable DOF of the current experimental design is mostly limited by the degree of momentum correlation. Although approximately  $100 \times 100$  pixels have been allocated for momentum measurement, effectively, the momentum resolution is only  $50 \times 50$  as the FWHM of the momentum correlations is 2.1 pixels wide. Using a laser with a longer coherence length of  $l_c = 2$  mm will be able to improve  $\sigma_{k_1+k_2}$  by a factor of 5 which would allow the full sensor area of the camera ( $256 \times 256$  pixels) to be effectively used for momentum measurement when two cameras are used as the experiment was initially designed.

### Digital Refocusing Procedure

Using the position and momentum information of each photon, the operation for digital refocusing of a sample placed out of focus by a distance  $z$  can be achieved using two steps. First, the trajectory of the photons are determined



through ray tracing using a ray transfer matrix

$$\begin{bmatrix} \vec{r}_2 \\ \vec{\theta}_2 \end{bmatrix} = \begin{bmatrix} A & B \\ C & D \end{bmatrix} \begin{bmatrix} \vec{r}_1 \\ \vec{\theta}_1 \end{bmatrix}, \quad (2)$$

where  $\vec{r}_1$  and  $\vec{r}_2$  are the positions of each photon pair detected at the two camera image planes,  $\vec{\theta}_1$  and  $\vec{\theta}_2$  are the angles at which the photons hit each plane and the ray transfer (ABCD) matrix is determined by the optical components placed between the two image planes. Since  $\vec{r}_1$  and  $\vec{r}_2$  are measured directly by the two cameras and the ABCD matrix is also known,  $\vec{\theta}_1$  and  $\vec{\theta}_2$  can be determined from Eq. (2). Knowing  $\vec{r}$  and  $\vec{\theta}$ , an appropriate ABCD matrix is then used to digitally propagate each photon to the location of the sample. The image obtained after this first step is the sample's diffraction pattern amplitude at a distance  $z$  when illuminated by a plane wave propagating in the  $z$ -direction (this is theoretically shown in the Supplementary Materials).

Next, a Gerchberg-Saxton type algorithm can be used to recover the amplitude of the sample if the sample has a uniform or known phase profile. The traditional Gerchberg-Saxton algorithm [37, 38] uses the amplitude information obtained at the image plane and Fourier plane to retrieve the phase information of the two through the Fourier transform relation between the two planes. Here, we use the amplitude of an arbitrary plane and the phase of another to retrieve the corresponding missing phase and amplitude of the two planes. The relationship between the two planes is no longer a direct Fourier transform but that of wave diffraction where techniques for approximating wave diffraction, such as the angular spectrum method or Fresnel diffraction method, must be used. The algorithm works as follows:

1. Guess an initial phase profile for the diffraction pattern amplitude obtained after ray tracing (a flat initial phase was used here).
2. Apply the angular spectrum method to the diffraction pattern to reverse diffraction and obtain an amplitude and phase profile of the sample (Fig. 2 b1 to b2).
3. Replace the phase profile of the sample obtained from 1. with the known phase profile (which is zero for the targets used in this experiment) and then apply the angular spectrum method to obtain the amplitude and phase of its diffraction pattern (Fig. 2 b2 to b3).
4. Update the diffraction pattern obtained from ray tracing with the new phase profile (Fig. 2 b3 to b4).
5. Repeat the process from step 2.

The angular spectrum method is applied as follows, for a beam with an initial amplitude and phase profile of  $U_i(x, y)e^{i\phi_i(x, y)}$ , the profile after propagating a distance  $z$  is

$$U_f(x, y)e^{i\phi_f(x, y)} = \mathcal{F}^{-1} \left[ \mathcal{F} \left( U_i(x, y)e^{i\phi_i(x, y)} \right) e^{ik_z z} \right], \quad (3)$$

where  $\mathcal{F}$  ( $\mathcal{F}^{-1}$ ) denotes the (inverse) Fourier transform operation and  $k_z = \sqrt{k^2 - k_x^2 - k_y^2}$  with  $k = 2\pi/\lambda$  being the photon wavenumber.

### Acknowledgements

The authors are grateful to Denis Guay, and Doug Moffatt for technical support. The authors acknowledge the support of Canada Research Chair, NRC-uOttawa Joint Centre for Extreme Quantum Photonics (JCEP), Quantum Sensors Challenge Program at the National Research Council of Canada and Defence Research and Development Canada.

- 
- [1] G. Brida, M. Genovese, and I. Ruo Berchera. Experimental realization of sub-shot-noise quantum imaging. *Nature Photonics*, 4:227, 2010.
- [2] Nigam Samantaray, Ivano Ruo-Berchera, Alice Meda, and Marco Genovese. Realization of the first sub-shot-noise wide field microscope. *Light: Science & Applications*, 6:e17005, 2017.
- [3] T. B. Pittman, Y. H. Shih, D. V. Strekalov, and A. V. Sergienko. Optical imaging by means of two-photon quantum entanglement. *Phys. Rev. A*, 52:R3429–R3432, Nov 1995.

- [4] Jeffrey H. Shapiro and Robert W. Boyd. The physics of ghost imaging. Quantum Information Processing, 11(4):949–993, Aug 2012.
- [5] Miles J. Padgett and Robert W. Boyd. An introduction to ghost imaging: quantum and classical. Philosophical Transactions of the Royal Society of London A: Mathematical, Physical and Engineering Sciences, 375(2099), 2017.
- [6] Magued B. Nasr, Bahaa E. A. Saleh, Alexander V. Sergienko, and Malvin C. Teich. Demonstration of dispersion-canceled quantum-optical coherence tomography. Phys. Rev. Lett., 91:083601, Aug 2003.
- [7] Pablo Yepiz-Graciano, Zeferino Ibarra-Borja, Roberto Ramírez Alarcón, Gerardo Gutiérrez-Torres, Héctor Cruz-Ramírez, Dorilian Lopez-Mago, and Alfred B. U'Ren. Quantum optical coherence microscopy for bioimaging applications. Phys. Rev. Applied, 18:034060, Sep 2022.
- [8] Andrei Nomerotski. Imaging and time stamping of photons with nanosecond resolution in timepix based optical cameras. Nuclear Instruments and Methods in Physics Research Section A: Accelerators, Spectrometers, Detectors and Associated Equipment, 937:26 – 30, 2019.
- [9] Hugo Defienne, Jiuxuan Zhao, Edoardo Charbon, and Daniele Faccio. Full-field quantum imaging with a single-photon avalanche diode camera. Phys. Rev. A, 103:042608, Apr 2021.
- [10] Yingwen Zhang, Duncan England, Andrei Nomerotski, Peter Svihra, Steven Ferrante, Paul Hockett, and Benjamin Sussman. Multidimensional quantum-enhanced target detection via spectrotemporal-correlation measurements. Phys. Rev. A, 101:053808, May 2020.
- [11] Jiuxuan Zhao, Ashley Lyons, Arin Can Ulku, Hugo Defienne, Daniele Faccio, and Edoardo Charbon. Light detection and ranging with entangled photons. Opt. Express, 30(3):3675–3683, Jan 2022.
- [12] Yingwen Zhang, Duncan England, and Benjamin Sussman. Snapshot hyperspectral imaging with quantum correlated photons. arXiv e-prints, page arXiv:2204.05984, April 2022.
- [13] Hazel Hodgson, Yingwen Zhang, Duncan England, and Benjamin Sussman. Reconfigurable phase contrast microscopy with correlated photon pairs. arXiv e-prints, page arXiv:2212.10918, December 2022.
- [14] Tomas Aidukas, Pavan Chandra Konda, Andrew R. Harvey, Miles J. Padgett, and Paul-Antoine Moreau. Phase and amplitude imaging with quantum correlations through fourier ptychography. Scientific Reports, 9(1):10445, Jul 2019.
- [15] Bienvenu Ndagano, Hugo Defienne, Dominic Branford, Yash D. Shah, Ashley Lyons, Niclas Westerberg, Erik M. Gauger, and Daniele Faccio. Quantum microscopy based on hong-ou-mandel interference. Nature Photonics, 16(5):384–389, May 2022.
- [16] Yingwen Zhang, Antony Orth, Duncan England, and Benjamin Sussman. Ray tracing with quantum correlated photons to image a three-dimensional scene. Phys. Rev. A, 105:L011701, Jan 2022.
- [17] E. H. Adelson and J. Y. A. Wang. Single lens stereo with a plenoptic camera. IEEE Transactions on Pattern Analysis and Machine Intelligence, 14(2):99–106, 1992.
- [18] R Ng, M Levoy, M Bredif, G Duval, M Horowitz, and P Hanrahan. Light field photography with a hand-held plenoptic camera, 2005.
- [19] <https://raytrix.de/>.
- [20] Marc Levoy, Ren Ng, Andrew Adams, Matthew Footer, and Mark Horowitz. Light field microscopy. ACM Transactions on Graphics, 25(3):924–934, 2006.
- [21] Oliver Bimber and David Schedl. Light-field microscopy: A review. Journal of Neurology & Neuromedicine, 4:1–6, 01 2019.
- [22] Depeng Wang, Zhijing Zhu, Zhongyuan Xu, and Diming Zhang. Neuroimaging with light field microscopy: a mini review of imaging systems. The European Physical Journal Special Topics, 231(4):749–761, May 2022.
- [23] A. Orth, M. Ploschner, E. R. Wilson, I. S. Maksymov, and B. C. Gibson. Optical fiber bundles: Ultra-slim light field imaging probes. Science Advances, 5(4):eaav1555, 2019.
- [24] David C. Schedl and Oliver Bimber. Volumetric light-field excitation. Scientific Reports, 6(1):29193, Jul 2016.
- [25] Young-Tae Lim, Jae-Hyeung Park, Ki-Chul Kwon, and Nam Kim. Resolution-enhanced integral imaging microscopy that uses lens array shifting. Opt. Express, 17(21):19253–19263, Oct 2009.
- [26] Antony Orth and Kenneth Crozier. Microscopy with microlens arrays: high throughput, high resolution and light-field imaging. Opt. Express, 20(12):13522–13531, Jun 2012.
- [27] Michael Broxton, Logan Grose, Samuel Yang, Noy Cohen, Aaron Andalman, Karl Deisseroth, and Marc Levoy. Wave optics theory and 3-d deconvolution for the light field microscope. Opt. Express, 21(21):25418–25439, Oct 2013.
- [28] Noy Cohen, Samuel Yang, Aaron Andalman, Michael Broxton, Logan Grose, Karl Deisseroth, Mark Horowitz, and Marc Levoy. Enhancing the performance of the light field microscope using wavefront coding. Opt. Express, 22(20):24817–24839, Oct 2014.
- [29] Xing Lin, Jiamin Wu, Guoan Zheng, and Qionghai Dai. Camera array based light field microscopy. Biomed. Opt. Express, 6(9):3179–3189, Sep 2015.
- [30] Changliang Guo, Wenhao Liu, Xuanwen Hua, Haoyu Li, and Shu Jia. Fourier light-field microscopy. Opt. Express, 27(18):25573–25594, Sep 2019.
- [31] Yi Zhang, Yuling Wang, Mingrui Wang, Yuduo Guo, Xinyang Li, Yifan Chen, Zhi Lu, Jiamin Wu, Xiangyang Ji, and Qionghai Dai. Multi-focus light-field microscopy for high-speed large-volume imaging. Photonix, 3(1):30, Nov 2022.
- [32] Milena D’Angelo, Francesco V. Pepe, Augusto Garuccio, and Giuliano Scarcelli. Correlation plenoptic imaging. Phys. Rev. Lett., 116:223602, Jun 2016.
- [33] Francesco V. Pepe, Francesco Di Lena, Augusto Garuccio, Giuliano Scarcelli, and Milena D’Angelo. Correlation plenoptic imaging with entangled photons. Technologies, 4(2), 2016.
- [34] Francesco Di Lena, Francesco V. Pepe, Augusto Garuccio, and Milena D’Angelo. Correlation plenoptic imaging: An

overview. *Applied Sciences*, 8(10), 2018.

- [35] Francesco V. Pepe, Francesco Di Lena, Aldo Mazzilli, Eitan Edrei, Augusto Garuccio, Giuliano Scarcelli, and Milena D’Angelo. Diffraction-limited plenoptic imaging with correlated light. *Phys. Rev. Lett.*, 119:243602, Dec 2017.
- [36] Gianlorenzo Massaro, Davide Giannella, Alessio Scagliola, Francesco Di Lena, Giuliano Scarcelli, Augusto Garuccio, Francesco V. Pepe, and Milena D’Angelo. Light-field microscopy with correlated beams for high-resolution volumetric imaging. *Scientific Reports*, 12(1):16823, Oct 2022.
- [37] R. W. Gerchberg and W. O. Saxton. Two-photon diffraction and quantum lithography. *Optik*, 35:237–246, Jan 1972.
- [38] J. R. Fienup. Phase retrieval algorithms: a comparison. *Appl. Opt.*, 21(15):2758–2769, Aug 1982.
- [39] G. Kim, K. Park, K.T. Lim, J. Kim, and G. Cho. Improving spatial resolution by predicting the initial position of charge-sharing effect in photon-counting detectors. *Journal of Instrumentation*, 15(01):C01034–C01034, Jan 2020.
- [40] Agedi N. Boto, Pieter Kok, Daniel S. Abrams, Samuel L. Braunstein, Colin P. Williams, and Jonathan P. Dowling. Quantum interferometric optical lithography: Exploiting entanglement to beat the diffraction limit. *Phys. Rev. Lett.*, 85:2733–2736, Sep 2000.
- [41] Milena D’Angelo, Maria V. Chekhova, and Yanhua Shih. Two-photon diffraction and quantum lithography. *Phys. Rev. Lett.*, 87:013602, Jun 2001.
- [42] Victor Vidyapin, Yingwen Zhang, Duncan England, and Benjamin Sussman. Characterisation of a single photon event camera for quantum imaging. *arXiv e-prints*, page arXiv:2211.13788, November 2022.
- [43] <https://global.canon/en/news/2021/20211215.html>.
- [44] <https://www.amscins.com/tpx3cam/>.
- [45] Arthur Zhao, Martin van Beuzekom, Bram Bouwens, Dmitry Byelov, Irakli Chakaberia, Chuan Cheng, Erik Maddox, Andrei Nomerotski, Peter Svihra, Jan Visser, Vaclav Vrba, and Thomas Weinacht. Coincidence velocity map imaging using tpx3cam, a time stamping optical camera with 1.5 ns timing resolution. *Review of Scientific Instruments*, 88(11):113104, 2017.
- [46] Hugo Defienne and Sylvain Gigan. Spatially entangled photon-pair generation using a partial spatially coherent pump beam. *Phys. Rev. A*, 99:053831, May 2019.

## Supplementary Materials

### Refocusing Operation

For a plane wave traveling in an arbitrary direction  $U(x, y, z) = Ae^{i(ux+vy+wz)}$  (with  $2\pi/\lambda = k = \sqrt{u^2 + v^2 + w^2}$ ) illuminating a target with complex spatial profile  $f(x, y) = \mathcal{F}^{-1}[F(k_x/2\pi, k_y/2\pi)]$  ( $\mathcal{F}$  denoting the Fourier transform operation) placed at  $z = 0$ , the transmitted wave can then be written as a superposition of plane waves (also known as the angular spectrum method) given by

$$\begin{aligned} U_T(x, y, z) &= \frac{1}{4\pi^2} \int \int_{-\infty}^{\infty} F(k_x/2\pi, k_y/2\pi) e^{i(k_x x + k_y y)} U(x, y, 0) e^{i\tilde{k}_z z} dk_x dk_y \\ &= \mathcal{F}^{-1} \left[ F(k_x/2\pi, k_y/2\pi) e^{i(\tilde{k}_z z)} \right] U(x, y, 0), \end{aligned} \quad (4)$$

with  $\tilde{k}_z = \sqrt{k^2 - (k_x + u)^2 - (k_y + v)^2}$ .

In the case of small angles approximation where the x and y components of the k-vector is much smaller than the z-component, we can approximate  $\tilde{k}_z$  using a Taylor series expansion

$$\begin{aligned} \tilde{k}_z &= \sqrt{k^2 - k_x^2 - k_y^2 - 2k_x u - 2k_y v - u^2 - v^2} \\ &\approx k_z - \frac{k_x u + k_y v}{k_z} + O(u^2, v^2), \end{aligned} \quad (5)$$

where  $k_z = \sqrt{k^2 - k_x^2 - k_y^2}$ .

Now substituting back into eq.4 we have

$$\begin{aligned} U_T(x, y, z) &\approx \mathcal{F}^{-1} \left[ F(k_x/2\pi, k_y/2\pi) e^{i\left(k_z - \frac{k_x u + k_y v}{k_z}\right)z} \right] U(x, y, 0) \\ &= \mathcal{F}^{-1} \left\{ \mathcal{F} [f(x - \Delta x, y - \Delta y)] e^{ik_z z} \right\} U(x, y, 0) \\ &= \tilde{f}(x - \Delta x, y - \Delta y, z) U(x, y, 0), \end{aligned} \quad (6)$$

where we have used the Fourier transform property  $\mathcal{F} [f(x - \Delta x)] = F(k_x/2\pi) e^{-ik_x \Delta x}$  with  $\Delta x = \frac{uz}{k_z}$  and  $\Delta y = \frac{vz}{k_z}$  and  $\tilde{f}(x, y, z) \equiv \mathcal{F}^{-1} \left\{ \mathcal{F} [f(x, y)] e^{ik_z z} \right\}$  is the diffracted field of a target  $f(x, y)$  illuminated by a plane wave traveling in the z-direction.

For this experiment, there are an infinite number of plane waves illuminating the target of which we are able to measure a total of  $N \times M$ , the total number of pixels used to capture the idler photons in the far-field plane, Thus we will denote the transmitted wave associated with a particular far-field pixel, with pixel index  $n$  and  $m$  in the  $x$  and  $y$  direction respectively, as  $U_{Tnm}(x, y, z) = \tilde{f}(x - \Delta x_n, y - \Delta y_m, z)U_{nm}(x, y, 0)$  with  $U_{nm}(x, y, 0) = A_{nm}e^{i(u_n x + v_m y)}$ . The captured image in the near-field plane  $I_0(x, y, z_0)$  is thus given by the sum of all the transmitted waves squared, i.e.

$$I_0(x, y, z_0) = \left| \sum_{n,m} \tilde{f}(x - \Delta x_n, y - \Delta y_m, z_0)U_{nm}(x, y, 0) \right|^2. \quad (7)$$

Since we can track each photon in forming  $I_0(x, y, z_0)$  from the far-field to the near-field plane, we can break up  $I_0(x, y, z_0)$  into a total of  $N \times M$  individual images  $\tilde{I}_{nm}(x, y, z_0)$  for each  $(u_n, v_m)$  pixel in the far-field thus

$$I_0(x, y, z_0) = \sum_{n,m} \tilde{I}_{nm}(x, y, z_0) = \left| \sum_{n,m} \tilde{f}(x - \Delta x_n, y - \Delta y_m, z_0)U_{nm}(x, y, 0) \right|^2. \quad (8)$$

Making a coordinate shift gives

$$\begin{aligned} \sum_{n,m} \tilde{I}_{nm}(x + \Delta x_n, y + \Delta y_m, z_0) &= \left| \sum_{n,m} \tilde{f}(x, y, z_0)U_{nm}(x + \Delta x_n, y + \Delta y_m, 0) \right|^2 \\ &= \left| \tilde{f}(x, y, z_0) \right|^2 \left| \sum_{n,m} U_{nm}(x + \Delta x_n, y + \Delta y_m, 0) \right|^2. \end{aligned} \quad (9)$$

On the left side of eq. 9, the operation of shifting each image  $\tilde{I}_{nm}$  by a distance of  $\Delta x_n = \frac{u_n z_0}{k_z}$  and  $\Delta y_m = \frac{v_m z_0}{k_z}$  in the  $x$ - $y$  plane is equivalent to the ray-tracing operation of shifting the position of each photon by the same factor based on the direction the photon is traveling given by  $\theta_x \approx \frac{u_n}{k_z}$  and  $\theta_y \approx \frac{v_m}{k_z}$  after propagating a distance  $z_0$ . On the right hand side, the first term is the intensity of the diffraction pattern of the target  $\left| \tilde{f}(x, y, z_0) \right|^2$  as if obtained when illuminated by a plane wave traveling in the  $z$ -direction. The second term is the intensity of the illuminating beam at  $z = 0$ ,  $\left| \sum_{n,m} U_{nm}(x + \Delta x_n, y + \Delta y_m, 0) \right|^2$ , with each plane wave also shifted by  $\Delta x_n$  and  $\Delta y_m$  in the  $x$ - $y$  plane. If the intensity of the illuminating beam is uniform across the target then,

$$\sum_{n,m} \tilde{I}_{nm}(x + \Delta x_n, y + \Delta y_m, z_0) \propto \left| \tilde{f}(x, y, z_0) \right|^2. \quad (10)$$

Thus, with the amplitude of the diffraction pattern known and if we also know the phase profile of the target, the amplitude of the target can be retrieved using a Gerchberg-Saxton type algorithm whose implementation is detailed in the main text.

## V. DEPTH OF FIELD OF A CONVENTIONAL MICROSCOPE

The depth of field for a conventional optical microscope is given by

$$\text{DOF} = \frac{n \cdot \lambda}{\text{NA}^2} + \frac{n \cdot e}{M \cdot \text{NA}}, \quad (11)$$

where, for this experiment,  $n = 1$  is the refractive index in air,  $\lambda = 810 \text{ nm}$  is the photon wavelength,  $\text{NA} = 0.45$  is the objective numerical aperture,  $M = 20$  is the magnification and  $e$  the distance resolved. So for  $e = 5 \mu\text{m}$  the DOF is  $4.6 \mu\text{m}$  and for  $e = 10 \mu\text{m}$  the DOF is  $5.1 \mu\text{m}$ , thus QCLFM has a DOF that is at least 2 orders of magnitude larger compared to a conventional microscope.

### Images of full dataset

All images for the dataset shown in Fig. 3(d) of the main manuscript is shown below in Fig. 7.

Fig. 8 shows the dataset when using a 35 mm focal length condenser lens instead of the 100 mm condenser lens as used for Fig. 7. This configuration was chosen such that the smallest resolvable feature at each distance is close to the resolution limit of the camera. With this configuration, at the objective focus, the field of view (FOV) is approximately 1/3 of that when using a 100 mm condenser lens. However, the FOV expands much more rapidly with the 35 mm lens allowing larger target feature to better fit into the FOV when far away from the objective focus.

In Fig. 8, we can see that beyond  $-200 \mu\text{m}$  away from the objective focus, the presence of the target can no longer be observed in the near field of the crystal plane imaged by the signal beam. From  $-2.8 \text{ mm}$  away from the objective focus, the presence of the target can once again be observed through ghost imaging in the far field of the crystal plane imaged by the idler beam. A plot showing the smallest resolvable features vs. the distance from focus is shown in Fig. 9.



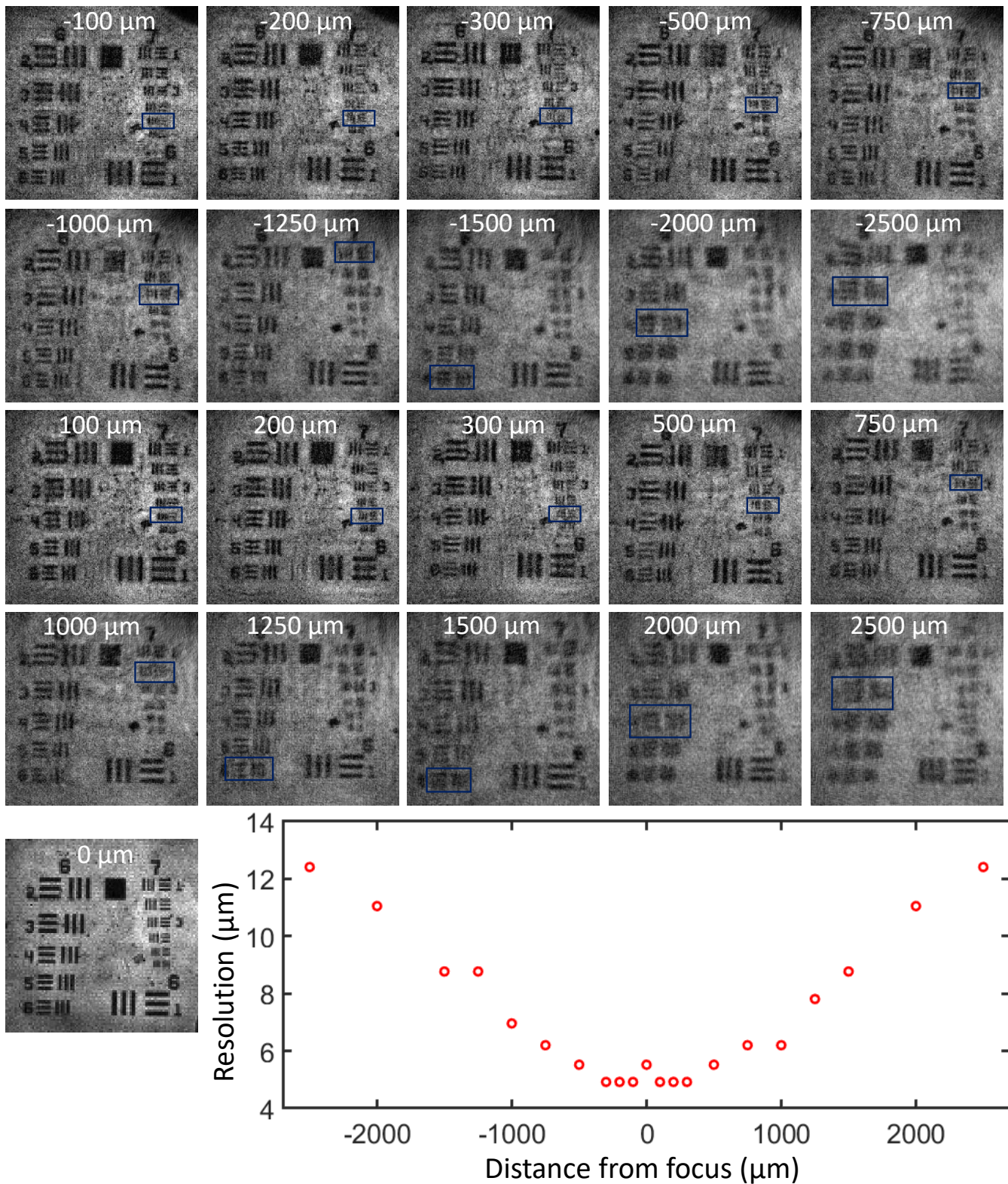


FIG. 7: Full dataset of Fig. 3 of the manuscript showing digitally refocused images of groups 6 and 7 of the 1951 USAF resolution target placed at various distances from the objective focus. The smallest resolvable features after refocusing are boxed in blue.



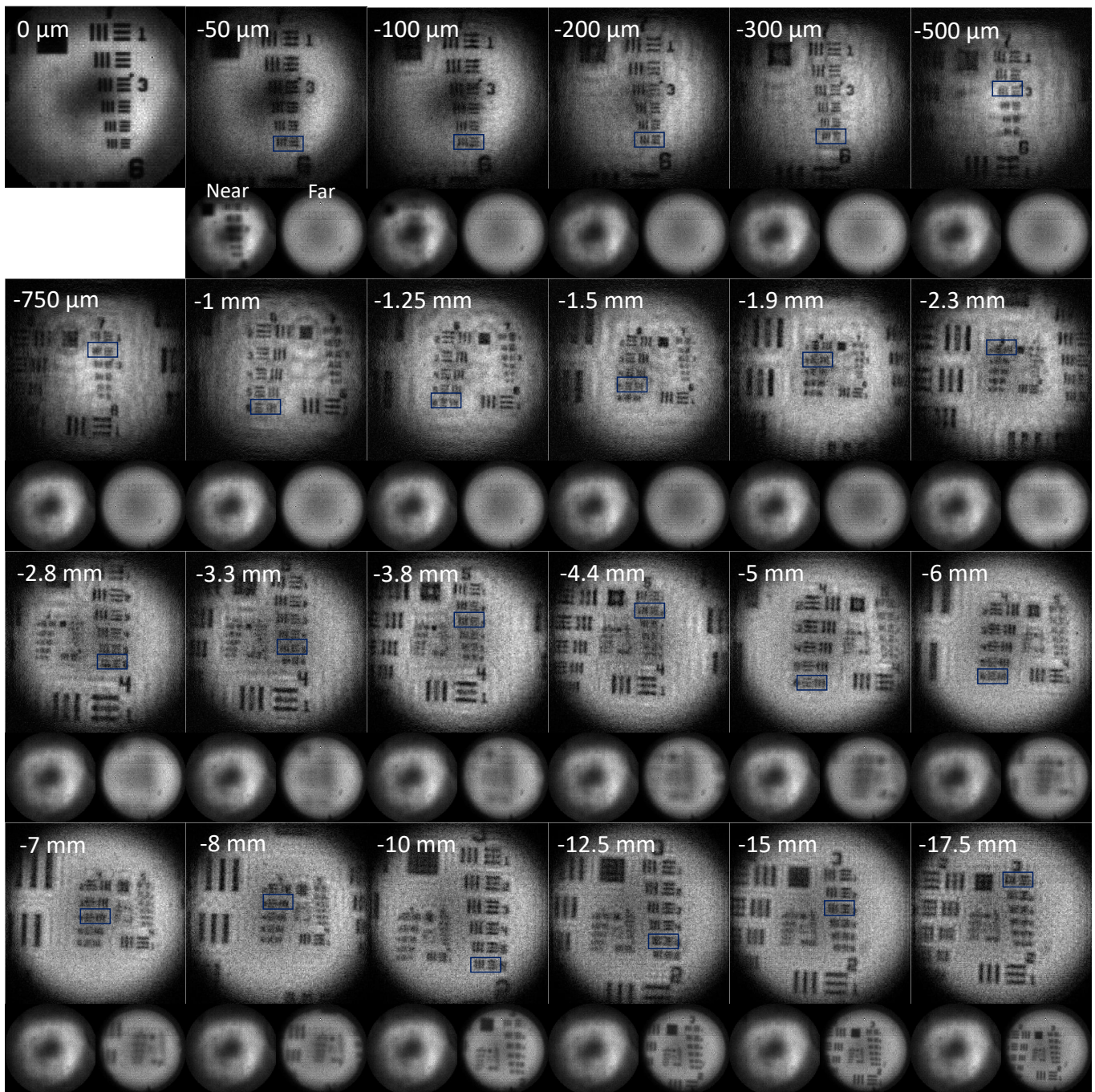


FIG. 8: Digitally refocused images of a 1951 USAF resolution target placed at various distances from the objective focus when using a 35 mm focal length condenser lens. The centred resolution target group from 0 to  $-750 \mu\text{m}$  away from the focus is group 7,  $-1 \text{ mm}$  to  $-2.3 \text{ mm}$  is group 6,  $-2.8 \text{ mm}$  to  $-4.4 \text{ mm}$  is group 5,  $-5 \text{ mm}$  to  $-7 \text{ mm}$  is group 4 and  $-10 \text{ mm}$  to  $-17.5 \text{ mm}$  is group 3. The smallest resolvable features after refocusing are boxed in blue. Images of the near field crystal plane, imaged by the signal beam, and far field crystal plane, imaged by the idler beam, before refocusing are shown below each refocused image.

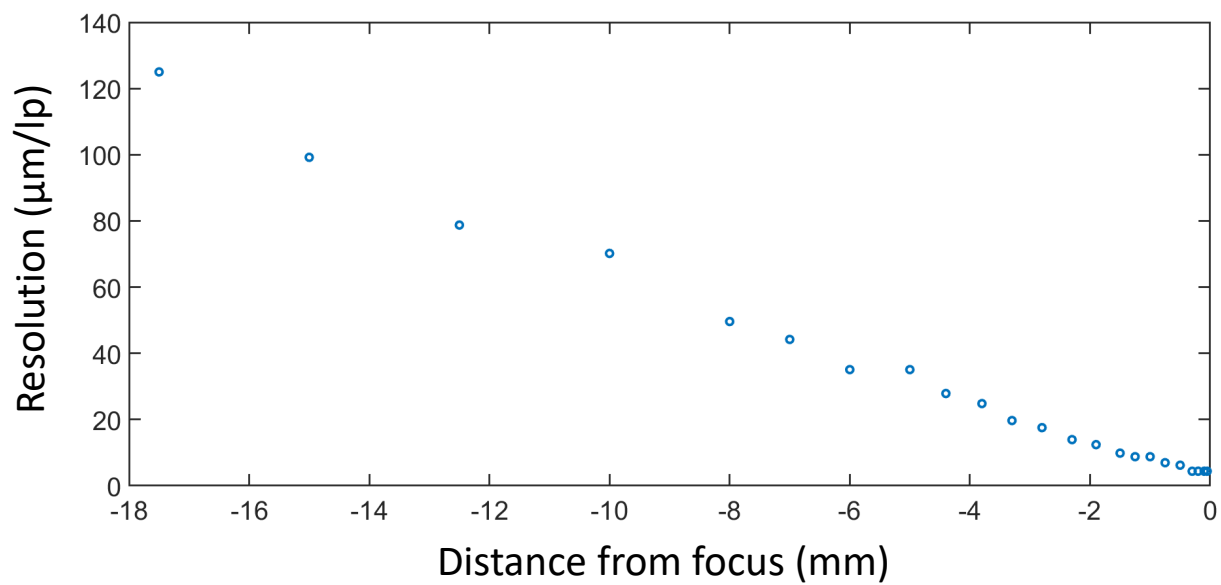


FIG. 9: Plot showing the smallest resolvable features vs. the distance from focus for data shown in Fig. 8.